

High Dispersion Optical Spectra of Nearby Stars Younger Than the Sun

Russel J. White¹, Jared M. Gabor², Lynne A. Hillenbrand

Department of Astronomy, California Institute of Technology, MS 105-24, Pasadena, CA 91125

russel.white@uah.edu, jgabor@orion.as.arizona.edu, lah@warning.caltech.edu

ABSTRACT

We present high dispersion ($R \sim 16,000$) optical (3900 – 8700 Å) spectra of 390 stars obtained with the Palomar 60-inch Telescope. The majority of stars observed are part of the Spitzer Legacy Science Program *The Formation & Evolution of Planetary Systems*. Through detailed analysis we determine stellar properties for this sample, including radial and rotational velocities, Li I λ 6708 and $H\alpha$ equivalent widths, the chromospheric activity index R'_{HK} , and temperature- and gravity-sensitive line ratios. Several spectroscopic binaries are also identified. From our tabulations, we illustrate basic age- and rotation-related correlations among measured indices. One novel result is that Ca II chromospheric emission appears to saturate at $v \sin i$ values above $\sim 30 \text{ km s}^{-1}$, similar to the well established saturation of x-rays that originate in the spatially separate coronal region.

Subject headings: stars: fundamental parameters — stars: activity — stars: pre-main sequence

1. Introduction

We have obtained high dispersion spectra of several hundred solar type stars within 20-160 pc of the Sun in order to determine fundamental stellar properties. Our work is in support of the *Spitzer*/Legacy Program “Formation and Evolution of Planetary Systems”

¹Present Address: University of Alabama in Huntsville, 301 Sparkman Dr., OB 201 B, Huntsville, AL 35899

²Present Address: University of Arizona, 933 N. Cherry Ave, Rm. N204, Tucson, AZ 85721

(FEPS; Meyer et al. 2006), which aims to understand the evolution of circumstellar dust from the primordial planet-building phase at an age of ~ 3 Myr to mature debris disk systems up to an age of ~ 3 Gyr. While data from the *Spitzer* Space Telescope probe the dust characteristics, a wide range of ancillary ground-based observations are required to estimate stellar properties. High dispersion spectroscopy, in particular, is a valuable tool for determining radial and rotational velocities, effective temperatures and surface gravities, abundances, and chromospheric activity diagnostics. These in turn provide useful constraints on stellar masses and ages. The stellar parameters derived from these spectroscopic observations thereby permit multiple axes of investigation for the infrared data from *Spitzer*, such as whether dust disk characteristics can be (anti-)correlated with stellar mass, signatures of youth, and/or stellar multiplicity.

In Section 2 we describe the observed sample and the spectroscopic observations. In Sections 3 and 4 we summarize the spectroscopic reductions and the methods used to extract spectroscopic properties. In Section 5 we discuss the spectroscopic binaries identified in the sample and illustrate basic age related correlations among the measured properties; the relation and apparent saturation of chromospheric Ca II emission versus projected rotational velocity is highlighted. The analysis is meant to be representative rather than complete. The spectroscopic properties are presented primarily to assist more detailed studies of individual FEPS stars.

2. Sample and Observations

Our primary sample for high dispersion spectroscopic observations consists of actual FEPS targets as well as many candidate targets eventually dropped from the FEPS program. The source list for FEPS is comprised of young near-solar analogs that range in mass from 0.7-1.5 M_{\odot} and span ages between 3 Myr and 3 Gyr. This source list was drawn from three samples of young solar-analogs. The first sample was assembled from the D. R. Soderblom (2000, private communication) volume-limited (< 50 pc) spectroscopic study of stars with B-V colors between 0.52 and 0.81 mag (spectral types F8-K0) and M_V magnitudes within 1.0 mag of the solar-metallicity zero-age main sequence; approximate ages are provided from the chromospheric activity index R'_{HK} . Since this nearby field sample primarily consists of stars older than a few $\times 10^8$ yr, a second sample was assembled with an targeted age range of 3-300 Myr. Stars in this sample were identified based on observational investigations to identify young main-sequence and pre-main sequence solar-type stars with strong x-ray emission, high lithium abundances, and kinematics appropriate for the young galactic disk (e.g. Mamajek et al. 2002). The third sample consists of stars in nearby well-

studied clusters, including 4 open clusters [IC 2602 (55 Myr), Alpha Per (90 Myr), Pleiades (125 Myr), Hyades (650 Myr)] and 3 younger T Tauri age clusters [R Corona Australis (3 Myr), Upper Scorpius (5 Myr), Upper Centaurus Lupus (10 Myr)]. Stars in these clusters serve to benchmark our field star selection criteria by providing sub-samples nearly identical in age, composition, and birth environment. These three parent samples and the procedure for downselecting to the final FEPS sample observed with *Spitzer* are described more fully in Meyer et al. (2006). In addition to stars in this primary sample, a handful of other young and/or chromospherically active stars (e.g. RS CVn) were observed for comparison, and ~ 20 stars with precisely known radial velocities (Nidever et al. 2002) were observed for calibration and analysis purposes.

High dispersion spectroscopic observations were obtained for 363 stars among the sample described above; 284 of these stars are among the 326 stars that comprise the final FEPS program as executed with *Spitzer* (the vast majority of FEPS stars not observed are in the southern hemisphere and thus inaccessible from Palomar Observatory). Fifty-two of the 363 stars observed are members of the 3 open clusters and 31 stars are members of the 3 young clusters. For calibration purposes, we also observed 13 giant stars with spectral types ranging from G5 to M2, 5 early- to mid-M dwarf stars, and 9 early A type stars with nearly featureless continua. Tables 1¹ and 2 list the observed sample (excluding non-solar type calibration stars), ordered by right ascension; Table 1 contains spectroscopic single stars and candidate single-lined spectroscopic binaries (for which stellar properties could be determined) while Table 2 contains known or newly discovered double-lined spectroscopic binaries. Coordinates for all stars are from the 2MASS All-Sky Catalog of Point Sources (Cutri et al. 2003), as interpreted by Vizier (Ochsenbein et al. 2000).

Spectroscopic observations were obtained on 9 observing runs between July 2001 and June 2003 with the Palomar 60-inch telescope and facility spectrograph (McCarthy 1988) in its echelle mode. This instrument is no longer available. A $1''.43 \times 7''.36$ slit was used, yielding spectra spanning from approximately 3900 Å to 8700 Å, with some small gaps between the redder orders. While the 2-pixel resolving power of this instrument is $\sim 19,000$, the achieved resolving power was typically $\sim 16,000$ because of image quality issues. The wavelength coverage was chosen so as to include both the Ca II H&K features at the blue end and the Ca II infrared-triplet at the red end. The spectrograph images the echelle spectra onto an 800×800 CCD; the consequence of projecting the broad wavelength coverage onto this modest sized CCD is that the orders are closely spaced, especially at the red end. The detector has a gain of 1.5 and read noise ~ 12 electrons. During each night of observations,

¹The complete version of Table 1 is available online.

series of bias exposures and flat field exposures were obtained to effect standard image processing. Because of the large spectral range of the instrument, the flat field images were taken with two separate incandescent lamps, one appropriate for illumination of the blueward range of the detector (at 60 seconds exposure time) and the other appropriate for the redward range (5 seconds exposure time). For wavelength calibration, spectra of Thorium-Argon lamps were obtained (45 seconds exposure time) generally before or after each on-sky group of target exposures,

Each target observation consisted of between 1 and 3 consecutive exposures. The dates for these observations are listed in Tables 1 and 2; multiple epoch observations are listed separately. At least 3 stars with precisely known radial velocities from Nidever et al. (2002) were observed per observing run.

One feature of this instrument is that the optimal focus for the bluest orders is not optimal for the reddest orders, so subjective compromises had to be made in focusing the spectrograph. Additionally, the spectroscopic focus was temperature sensitive, and therefore had to be tuned periodically throughout the night to achieve the best spectral resolution. On the night of 2002 Feb 2, many spectra were obtained at an exceptionally poor focus setting. When poorly focused, the spectrograph produces spectra that are stigmatic - spectral lines skewed relative to the dispersion direction which degrades resolution (by an amount that is wavelength dependent). To help assess how poor focus may compromise the analysis (e.g. $v\sin i$ measurements), on the night of 2002 Sep 18 we observed the radial velocity standard HD 164992 over a broad range of focus values.

3. Spectroscopic Reductions

3.1. Image Processing

Raw data frames were processed using tasks in IRAF and custom IDL scripts. First, the detector bias was removed. Although the bias pattern appeared to be stable during the course of an observing run, the absolute bias level drifted substantially on time scales of hours, changing by as much as 30% over the course of a night. Bias subtraction was performed, therefore, in a two-step process. First, the bias sequence obtained on each night was median combined using the IRAF “zerocombine” task, rejecting the highest and lowest valued bias images. Second, since the detector bias level for a given image may have drifted from the median value determined at the beginning or end of the night, a bias scaling factor was also determined. This was done by measuring the median pixel value within a specified area in the most poorly illuminated, inefficient portion of the array, located well below 3600

Å where useful spectra could not be extracted; even the brightest, bluest stars observed on our program showed essentially zero counts above bias in this portion of the array. For each target image, the median bias image from the beginning or end of the night was scaled by this factor and then subtracted.

Next, images were trimmed to exclude two unilluminated columns at the rightmost edge of the array. Cosmic ray events were removed using IRAF’s “cosmicrays” task and fairly liberal parameter settings that restricted the corrections to only bona fide cosmic rays.

The blue and red flat field sequences from each night were median combined using IRAF’s “flatcombine” procedure with sigma clipping. The blue and red medians were then stitched together approximately 1/3 of the way up the detector (at line 250) which has the effect of distorting the one (curved) spectral order which intersects this line. IRAF’s “apflatten” task was used to normalize the combined flat for each night by fitting its intensity along the dispersion using a low order (typically 3) polynomial while setting all pixels outside an order to unity. Flat fielding was performed by dividing each image by the normalized flat field image using IRAF’s “ccdproc” task.

Cosmetically, the images contain “tadpole streaks” of high count levels, comprised of short “heads” along the dispersion direction and then decaying count levels along long, mostly single pixel, “tails” perpendicular to the dispersion direction which thus affect multiple orders. The number of such defects per image was related to exposure time. A custom procedure was developed to crawl down each column comparing values on either side of the column and thus identifying these features. The pixels in the tail of the streak and a small square around the tadpole head were interpolated over.

The close spacing of the spectral orders did not permit measurement or removal of scattered light, an effect common in echelle spectrographs. However, comparisons of our extracted spectra with spectra previously obtained with other instruments (Section 3.2) and of measured equivalent widths with those from the literature (Section 4.1) suggest that the majority of excess flux caused by scattered light is removed during background subtraction.

3.2. Spectral Extraction and Wavelength Calibration

One dimensional spectra were extracted from the processed two dimensional images using IRAF’s “doeclit” task. Sixty orders were identified over the 800 x 800 pixel² array. A moderate (9th) order trace was employed and the spectra in each order were summed over 3-5 pixels perpendicular to the dispersion. Variance weighting was used for “optimal” extraction. The small separation between orders made removal of background and scattered

light especially challenging. After exploring a variety of methods for accomplishing this, the most robust method identified was simply to subtract the average minimum value within 2 background regions, one on each side of the spectrum. Aperture definition, background region definition, and order tracing were attended as opposed to automated processes.

To test the accuracy of the adopted background/scattered light subtraction, Jeff Valenti kindly provided a careful comparison of our spectra with spectra obtained with the HIRES spectrograph (Vogt et al. 1994) on the W. M. Keck I Telescope. The widely spaced orders of HIRES permit accurate background and scattered light corrections. These comparisons demonstrated that the average scattered and/or background light remaining in our spectra is approximately 4% at 3900 Å, and drops roughly linearly to 0% at 6200 Å. The implication is that equivalent widths of features at blue wavelengths may be diminished by a small amount. Rather than attempt to correct for this in the reduction process, we account for this in the relative calibration of properties extracted from blue wavelength features (Sections 4.3 and 4.4).

Although multiple Thorium-Argon spectra per night were obtained (often one for each star observed), in practice we established wavelength calibration as follows. The extraction trace defined by a single bright star on each night was applied to its corresponding Thorium-Argon exposure to extract a one-dimensional wavelength reference spectrum. A wavelength solution was determined using the “ecidentify” task in IRAF, and this solution was applied to all spectra for a given night. This established wavelength solution was then interpolated onto a log-linear scale.

From analysis of spectra taken on the same night, small spectral shifts of ~ 0.1 Å were common, as inferred from comparisons of the location of telluric absorption lines. These shifts were likely due to flexure of the instrumental optics with telescope pointing, and consequently resulted in wavelength solution offsets of this order for many spectra. As discussed below, this wavelength offset is accounted for in determining radial velocities by cross-correlating telluric features.

4. Spectroscopic Properties

Figure 1 shows portions of the echelle spectra for 7 stars near the Ca II H&K, Li I $\lambda 6708$ Å, and H α features. To help assess the quality of the spectra, two signal-to-noise ratios (SNRs) are estimated, one at ~ 6700 Å and one at ~ 3950 Å (labeled as Li and HK, respectively). The SNR at 6700 Å is determined from the gain-corrected median signal within the central portion of this order. The SNR at 3950 Å is determined similarly, but is

based the average of the values determined for the two adjacent orders containing the Ca II H (3968 Å) and K (3934 Å) features, and thus represent an approximate average over the continuum and broad absorption. These estimates are valid above values of $\gtrsim 20$, in which the noise is dominated by photon statistics. Lower values may actually over-estimate the SNR, because of the increased relative error in the background, scattered light and bias level subtractions (Section 3.1). The SNR distribution at 6700 Å is shown in Figure 2.

The following sections described the procedures used to extract stellar properties from these spectra. In comparisons with previous measurements, values determined in this study are referred to as P60 values. Specifically, equivalent widths (EWs) of Li I $\lambda 6708$ Å and H α are measured in Section 4.1, radial and rotational velocities are determined in Section 4.2, temperature and surface gravity indices are discussed in Section 4.3, and measured S values and calculated R'_{HK} indices are presented in Section 4.4.

4.1. Equivalent Widths of Li I 6708 Å and H α

Equivalent widths of the Li I $\lambda 6708$ Å doublet ($\lambda 6707.76$, $\lambda 6707.91$), which is spectroscopically unresolved in our observations, and H α ($\lambda 6562.8$ Å) are measured for all spectra using the *splot* task within *IRAF*. For measurement of the Li I absorption feature which is located near the peak of the blaze function in these spectra, the local continuum is determined by fitting a legendre polynomial to a ~ 30 Å portion of the spectrum, excluding values less than 2σ below the continuum (e.g. stellar absorption features) or more than 4σ above the continuum (e.g. noise spikes) in this fit. The order of the polynomial is varied (typically from 4 to 7) to best match the local continuum. With the continuum defined in this way, the EW values are determined by fitting a Gaussian profile to the absorption feature. Multiple measurements on a single night are averaged, while separate epochs are listed independently. If no feature is discernable in the spectrum, upper limits are determined from the noise in the local continuum. Table 1 lists the measured values.

The measured Li I EW values include a contribution from an Fe I line at 6707.441 Å. Soderblom et al. (1993) find that the strength of this temperature sensitive Fe I feature varies with $B - V$ color as $\text{EW}[\text{Fe I } \lambda 6707.441] = 20(B - V) - 3 \text{ m}\text{\AA}$. Since the $B - V$ values of most stars are known or can be estimated (Section 4.4), the contribution of this Fe I line to the Li I EW values can be removed.

To assess possible systematic uncertainties caused by the subjective aspects involved in measuring EW values (e.g. continuum determination) or instrumental effects, we compare our measurements to previous values determined from high dispersion spectroscopy. Of the

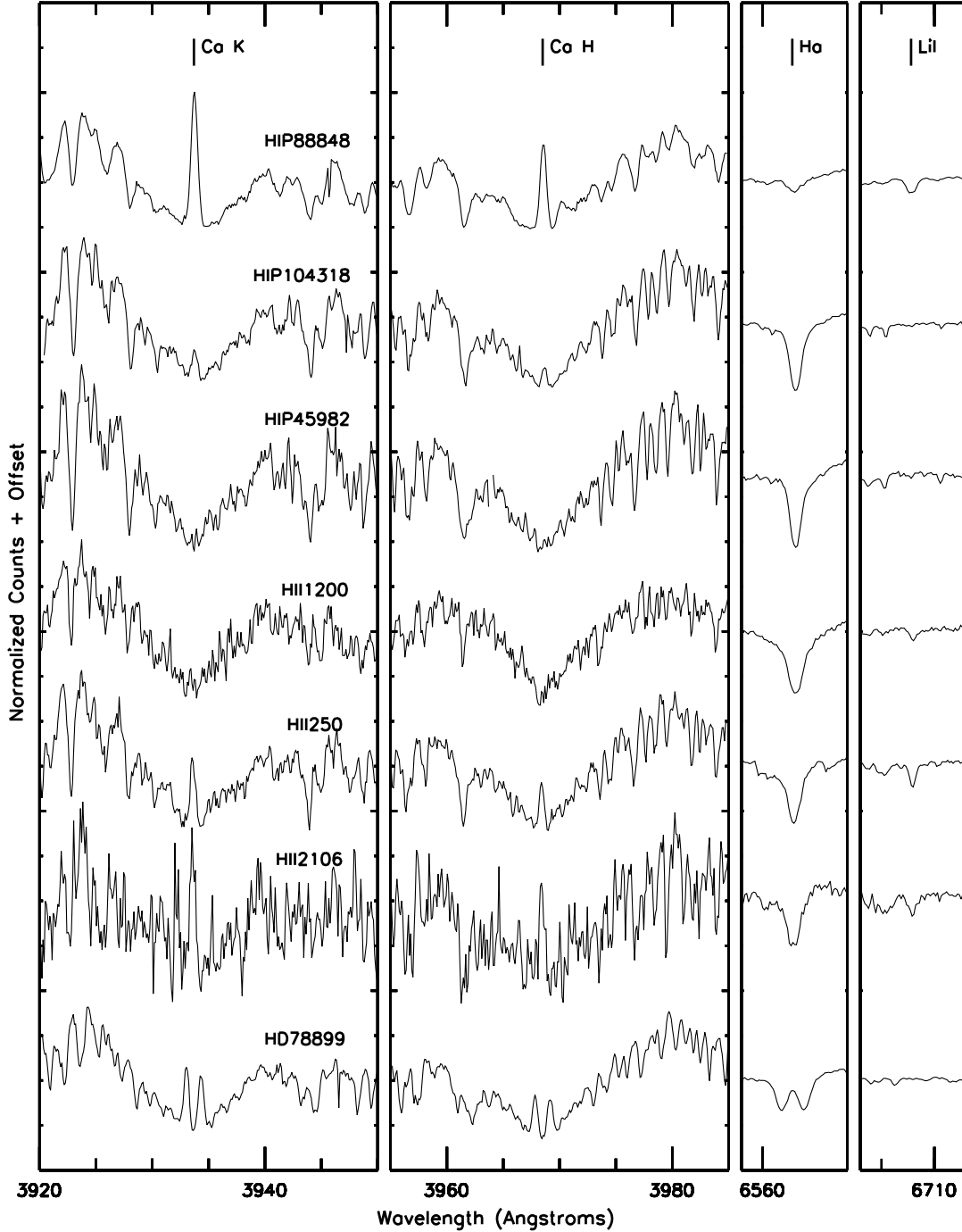


Fig. 1.— Portions of the extracted spectra. The top 3 spectra are G5 stars with decreasing levels of CaII H&K emission ($\log R'_{HK} = -4.13, -4.59, -5.01$). The next 3 spectra are Pleiads (and thus coeval), with spectral types of F5 (HII 1200), G2 (HII 250), and K0 (HII 2106). With a SNR of only ~ 18 in the CaII region, HII 2106 is typical of the poorest quality spectra from which $\log R'_{HK}$ values can be extracted; strong core emission can be seen in this case. The bottom spectrum shows the spectroscopic binary HD 78899, whose features are clearly doubled.

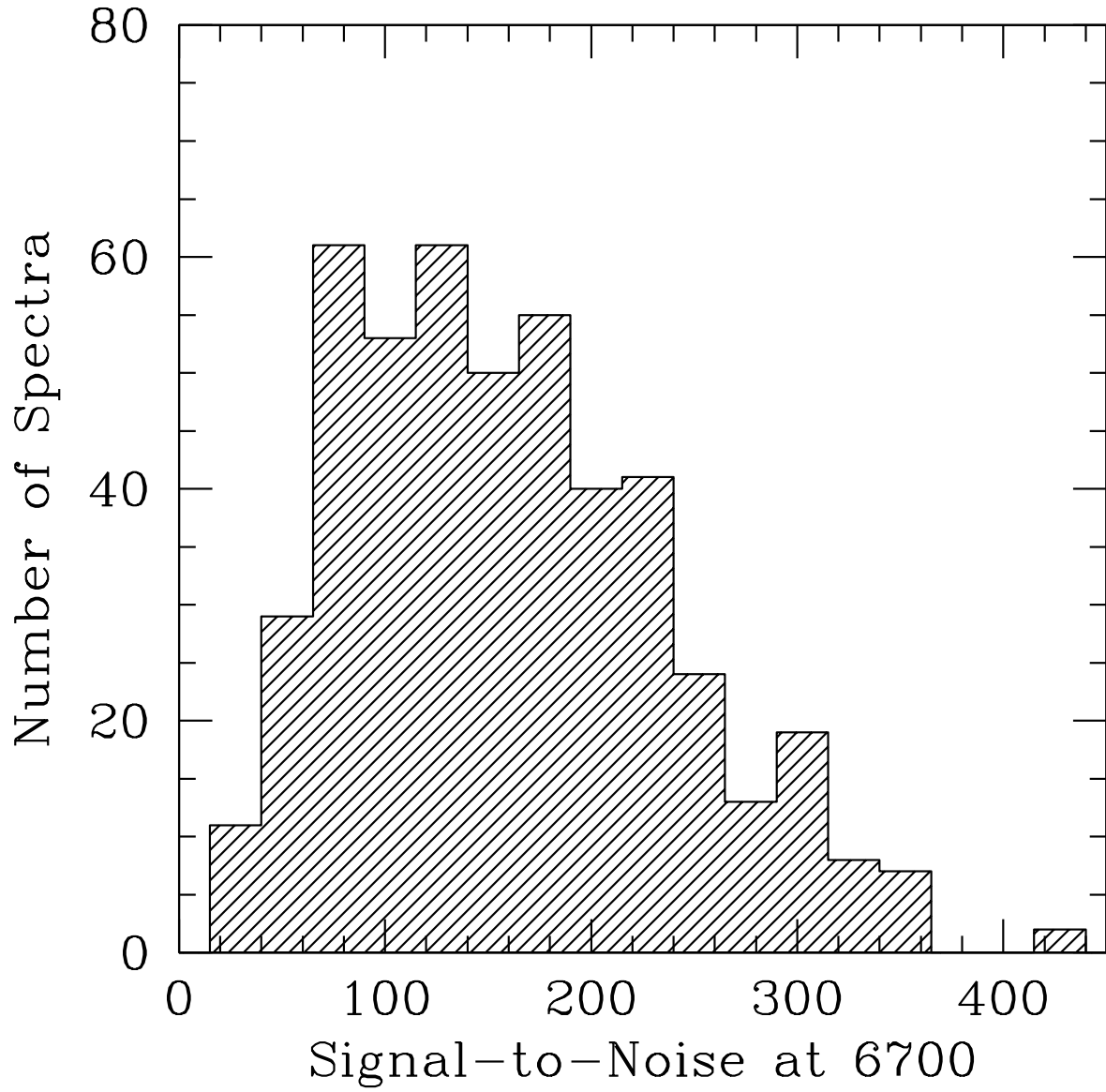


Fig. 2.— Signal-to-Noise distribution of all spectra obtained (includes multiple measurements and stars observed for calibration) of the 390 unique targets.

spectroscopically single stars observed here, 21 Pleiads were observed by Soderblom et al. (1993, $R = 50,000$), 19 Hyads were observed by Thorburn et al. (1993, $R = 26,000 - 32,000$), 26 field stars were observed by Wichmann et al. (2003, $R = 40,000$), and 28 field stars were observed by Strassmeier et al. (2000, $R = 25,000$). The uncertainties in the EW[Li]s from these previous studies are typically 5-10 mÅ. Of these 94 stars, 19 were observed twice by us, yielding a total of 113 measurements for comparison. Figure 3 shows the difference between the P60 and previous EW values; all values are as measured and thus uncorrected for the contamination of the Fe I line. Overall the agreement is good. The average and/or median difference for any of the 4 studies is ± 15 mÅ, with standard deviation of differences that range from 16 - 21 mÅ. The average difference with the entire comparison sample is -8 mÅ with a standard deviation of 20 mÅ. We conclude that any systematic bias in our measurements is $\lesssim 10$ mÅ. We adopt a uniform uncertainty of 0.02 Å.

For H α EWs, considerable care had to be taken both in normalizing to the local continuum and in fitting a functional form to the line profiles because of the broad wings. The local continuum was determined by fitting a legendre polynomial generally of order 10 to the entire spectral order, excluding values less than 2σ below or more than 4σ above the continuum. The procedure varied slightly as dictated by the noise level in the data, by the line breadth (because of, for example, rapid rotation), or if H α was found to be in emission. Both the sigma-rejection limits and the fitting order were modified in these cases to optimize the continuum fit. The EW values were determined by fitting a Voigt profile to the absorption feature; in a few cases of dramatically filled in H α , direct integration was used to determine the EW rather than function fitting. EWs are listed in Table 1; negative values indicate H α emission.

Four stars (HD 143006, RX J1842.9-3532, RX J1852.3-3700, LH98 196) show especially strong H α emission (> 10 Å); their H α profiles are shown in Figure 4. In these cases, the strength and breadth of these emission-line profiles are greater than that expected from chromospheric activity alone, and more consistent with that expected from the accretion of circumstellar material (e.g. Muzerolle et al. 1998; White & Basri 2003). We suggest that these stars are accreting.

For the 8 stars identified as double-lined spectroscopic binaries, EW[Li I]s and EW[H α]s for the individual components were determined by fitting two Gaussian profiles to the doubled features, when possible. For these pairs, we also measured EWs of the temperature sensitive Ca I $\lambda 6717$ Å feature, which can be used to identify better the primary and the secondary. The EW values for the binaries are listed in Table 2.

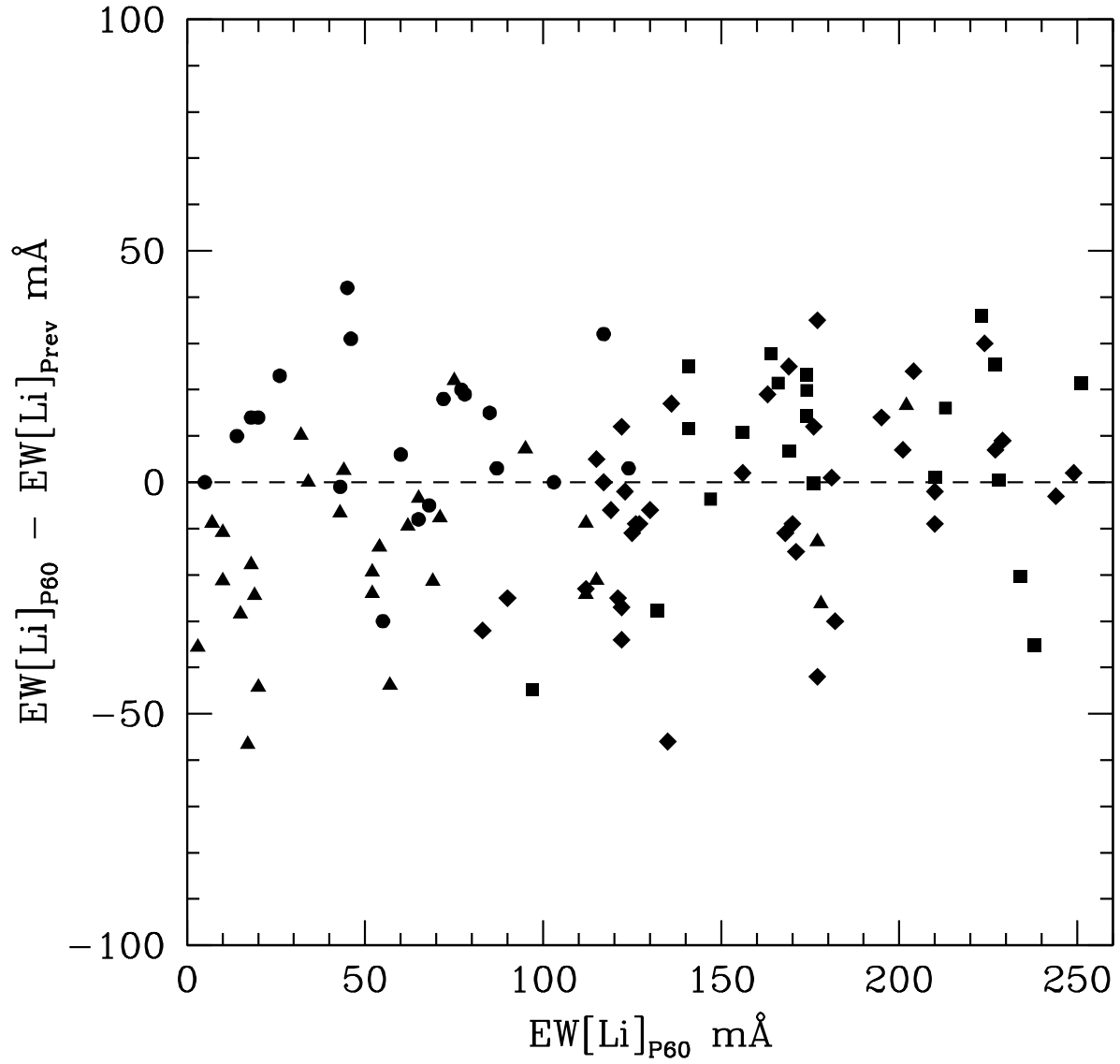


Fig. 3.— Comparison of measured $EW[LiI \lambda 6708 \text{ \AA}]$ values with values from (Soderblom et al. 1993, *squares*), (Thorburn et al. 1993, *circles*), (Wichmann et al. 2003, *diamonds*), and (Strassmeier et al. 2000, *triangles*).

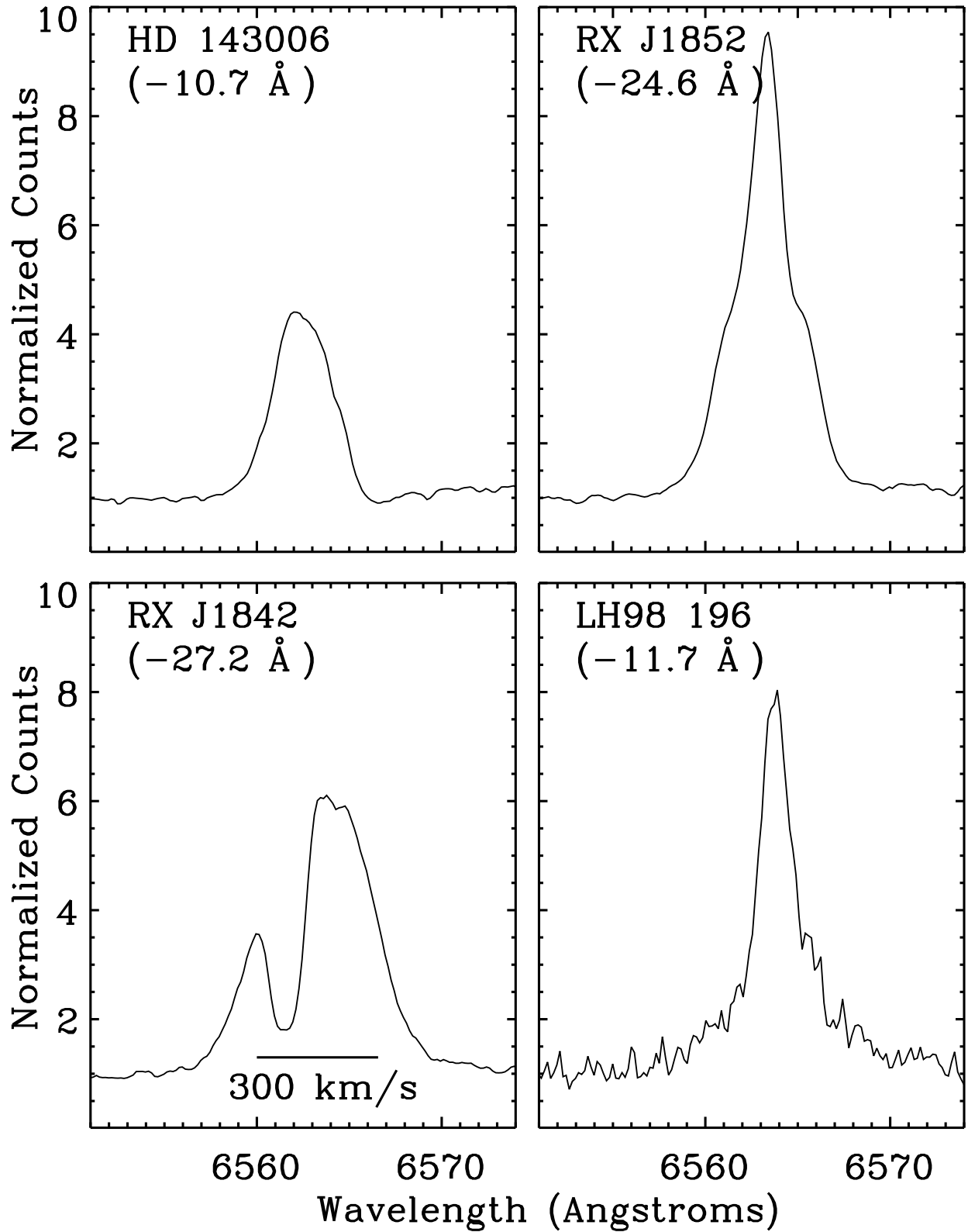


Fig. 4.— H α profiles for the 4 strong emission-line stars normalized by the local continuum; the H α equivalent width for each star is given in parentheses. A velocity width of 300 km s $^{-1}$ is indicated.

4.2. Radial and Rotational Velocities

Radial velocities and projected rotational velocities are determined via a cross-correlation analysis similar to that of White & Hillenbrand (2004). The analysis is restricted to the 36 orders spanning from ~ 4000 - 7500 \AA , excluding the 3 orders containing the telluric B-band, $H\alpha$, and Na II D features; orders at longer wavelengths have poorer wavelength solutions and those at shorter wavelengths typically have low SNRs. From this restricted range, orders having an average SNR greater than ~ 25 are then cross-correlated with the spectral orders of at least 3 slowly rotating comparison standards that have radial velocities accurate to $0.3 - 0.4 \text{ km s}^{-1}$ (Nidever et al. 2002). The radial velocity, relative to each standard, is then determined from the average velocity offset measured from all orders.

To determine the heliocentric radial velocities of the stars, the relative radial velocity must be corrected for barycentric motions and possible errors in the wavelength solution of either the standard or target spectrum. The former is determined using the *rvcorrect* task in IRAF. The latter correction is determined by cross-correlating the telluric A- and B-bands of the standard and the target star; the telluric correlations would yield an offset of zero for perfect wavelength calibration, but are typically $1\text{-}3 \text{ km s}^{-1}$ for the spectra analyzed here. The multiple heliocentric radial velocity estimates, determined from multiple radial velocity standards, are then averaged to find the final radial velocity.

Uncertainties in the radial velocities are estimated from a combination of statistical and empirical error estimates. First, the uncertainty in the radial velocity relative to each standard is assumed to be the uncertainty in the mean value of all orders used, combined with the uncertainty in the radial velocity of the standard (typically 0.3 km s^{-1}). The radial velocity estimates from all standards are then combined using a weighted average; the resulting statistical uncertainties are typically small ($0.1 - 0.3 \text{ km s}^{-1}$). As an empirical check on these uncertainty estimates, the radial velocity of each standard is determined from all other radial velocity standards observed during that run and compared to its assumed value. The average agreement of the radial velocity standards is typically a couple times larger than the statistical uncertainties, except in low SNR cases where the statistical uncertainty dominates. This suggests there may be systematic effects unaccounted for in the statistical uncertainty estimates. Thus, we combine the statistical uncertainty with this empirical uncertainty to determine final (conservative) radial velocity uncertainty estimates given in Table 1. Figure 5 shows the distributions of radial velocities for the field, open cluster, and young cluster samples.

Rotational velocities ($v\sin i$) for the observed targets are determined from the width of the peak in their cross-correlation with a slowly rotating standard. Specifically, the peak is fit by a parabola with the fitted width at half-peak maximum. To convert this width

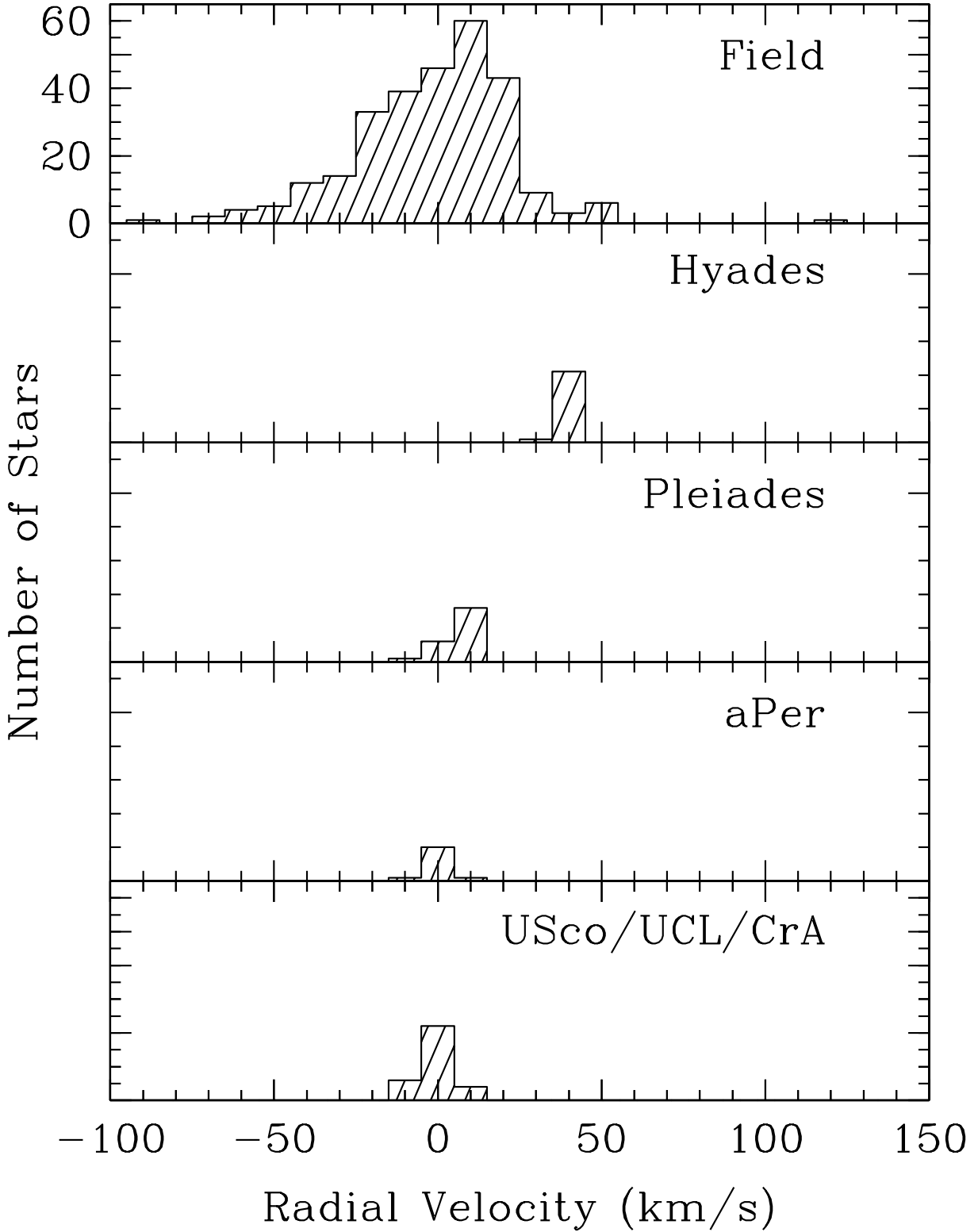


Fig. 5.— Distributions of radial velocities of the observed sample. The top panel shows the distribution for field stars and the bottom four panels show the distributions for cluster stars.

to a $v\sin i$ value, an empirical width versus $v\sin i$ relation is determined by cross-correlating many artificially “spun-up” spectra with the same slowly rotating standard. These artificially broadened spectra are constructed using the rotational profiles given in Gray (1992, $\epsilon = 0.6$). This procedure is computed for each order, yielding a $v\sin i$ estimate for each order. For each standard used, a $v\sin i$ value is computed from the median of all order estimates; a median is preferred since the $v\sin i$ measurements are often upper limits.

Uncertainties in $v\sin i$ are determined first from the standard deviation of the multiple $v\sin i$ measurements provided by all standards used. For observations consisting of multiple exposures, the uncertainty is the average standard deviation of these measurements. The $v\sin i$ values are assumed to be upper limits if less than 10 km s^{-1} (just over one-half the velocity resolution), or if $v\sin i$ is less than 3 times the uncertainty in $v\sin i$. We find that all templates of F, G, and K spectral types give consistent $v\sin i$ values; an exact match in spectral type is not critical in determining $v\sin i$.

As noted in the introduction, poor focus plagued some of our measurements, especially on the night of 2002 Feb 2. To assess how this may affect inferred properties, the above radial velocity and rotational velocity analysis was conducted on the observations of radial velocity standard HD 164922 observed at multiple focus settings (Section 2). Fortunately the inferred radial velocities for modest focus offsets, typical of changes over a given night, agree with the nominal value to $\sim 1 \text{ km s}^{-1}$, consistent with the inferred uncertainties. For extreme focus offsets, however, the discrepancy can be as large as 3 km s^{-1} . Similarly, for modest focus offsets from nominal, the inferred $v\sin i$ values would increase modestly, but since the standard deviation of measurements among the orders correspondingly increased, the end result is simply larger upper limits (e.g. $< 16 \text{ km s}^{-1}$ for HD 164922, compared with < 10 when observed at nominal focus). However, for extreme focus offsets, the spectroscopic blurring resulted in a large apparent $v\sin i$ (e.g. $22.0 \pm 3.3 \text{ km s}^{-1}$ for HD 164922). Since the majority of our spectra have at most only modest focus errors, no correction for this is made. Rotational velocities inferred from observations made on 2002 Feb 2, however, are marked with a colon in Table 1 as likely being artificially too large.

To empirically assess systematic errors in our radial and rotational velocity measurements, our values are compared with values measured by Nordstrom et al. (2004, which appeared after all of our data were taken). There are 135 stars in common between the surveys that (1) are not previously identified spectroscopic binaries, (2) are not used as radial velocity standards by us, and (3) have radial velocity uncertainties less than 4 km s^{-1} . Figure 6 shows the difference between our radial velocities and those of Nordstrom et al. (2004). The agreement is quite good; the average difference is -0.2 km s^{-1} with a standard deviation of 2.4 km s^{-1} . With the exception of 2 stars, HIP 67904 and HIP 61072, all measured radial

velocity values agree to within 10 km s^{-1} . HIP 67904 and HIP 61072, on the other hand, have significantly different radial velocity measurements ($> 25\sigma$ difference). As discussed below, we suggest these stars are spectroscopic binaries. This comparison also demonstrates that the radial velocities of stars with $v\sin i$ values as large as 45 km s^{-1} can be measured without significantly degraded precision.

In Figure 7 are shown Nordstrom et al. (2004) $v\sin i$ values versus the P60 $v\sin i$ values for the overlapping sub-sample described above. While Nordstrom et al. (2004) report $v\sin i$ values as low as 0 km s^{-1} (which is likely unrealistic), our lower resolution data restrict us to $v\sin i$ upper limits of 10 km s^{-1} or greater. The majority of our $v\sin i$ upper limits are thus greater than the values measured by Nordstrom et al. (2004), which inhibits interpretation of an overall comparison. However, a comparison of the 22 stars with measured values, however, suggests a systematic difference. The P60 $v\sin i$ values are larger, in the median, than those of Nordstrom et al. (2004) by 8.6 km s^{-1} . A portion of this difference may be a consequence of the spectroscopic blurring caused by the focus errors discussed above. When the 3 measured values from 2002 Feb 2 are removed, the P60 values are then larger by only 6.3 km s^{-1} , in the median. However, an independent comparison of the 389 stars with $v\sin i$ measurements in both Nordstrom et al. (2004) and Strassmeier et al. (2000), upper limits excluded, indicate the Nordstrom et al. (2004) values are less than the Strassmeier et al. (2000) values by 2.6 km s^{-1} . Thus, a portion of the difference with our measurements may be a consequence of artificially low values reported by Nordstrom et al. (2004). Overall we conclude that the majority of our measured $v\sin i$ values suffer from no systematic biases greater than $\sim 5 \text{ km s}^{-1}$. The exceptions are stars observed on 2002 Feb 2, which may be biased toward artificially large values by $\sim 10 - 20 \text{ km s}^{-1}$ because of especially poor focus. Since we are uncertain what the systematic correction to the $v\sin i$ values for these stars should be, if any, we make no correction for this in the values presented in Table 1.

4.3. Temperature and Gravity Indicators

Within the broad wavelength coverage provided by our echelle spectra are many temperature- and gravity-sensitive lines. Empirically, we find that the EWs of the photospheric features Fe I $\lambda 4063$, Fe I $\lambda 4071$, and Ca II $\lambda 4226$ (see Jaschek & Jaschek 1987) are especially useful temperature diagnostics. In our data, these features all increase in strength in a roughly linear fashion from spectral types F8 to K5, before degenerate flattening and turnover occurs towards later spectral types. However, fits of the EWs versus $B - V$ color for main sequence stars (not shown here) are accurate to only 0.05-0.1 in $B - V$. This implies that if we were to attempt spectral classification from the EWs, spectral type uncertainties of more

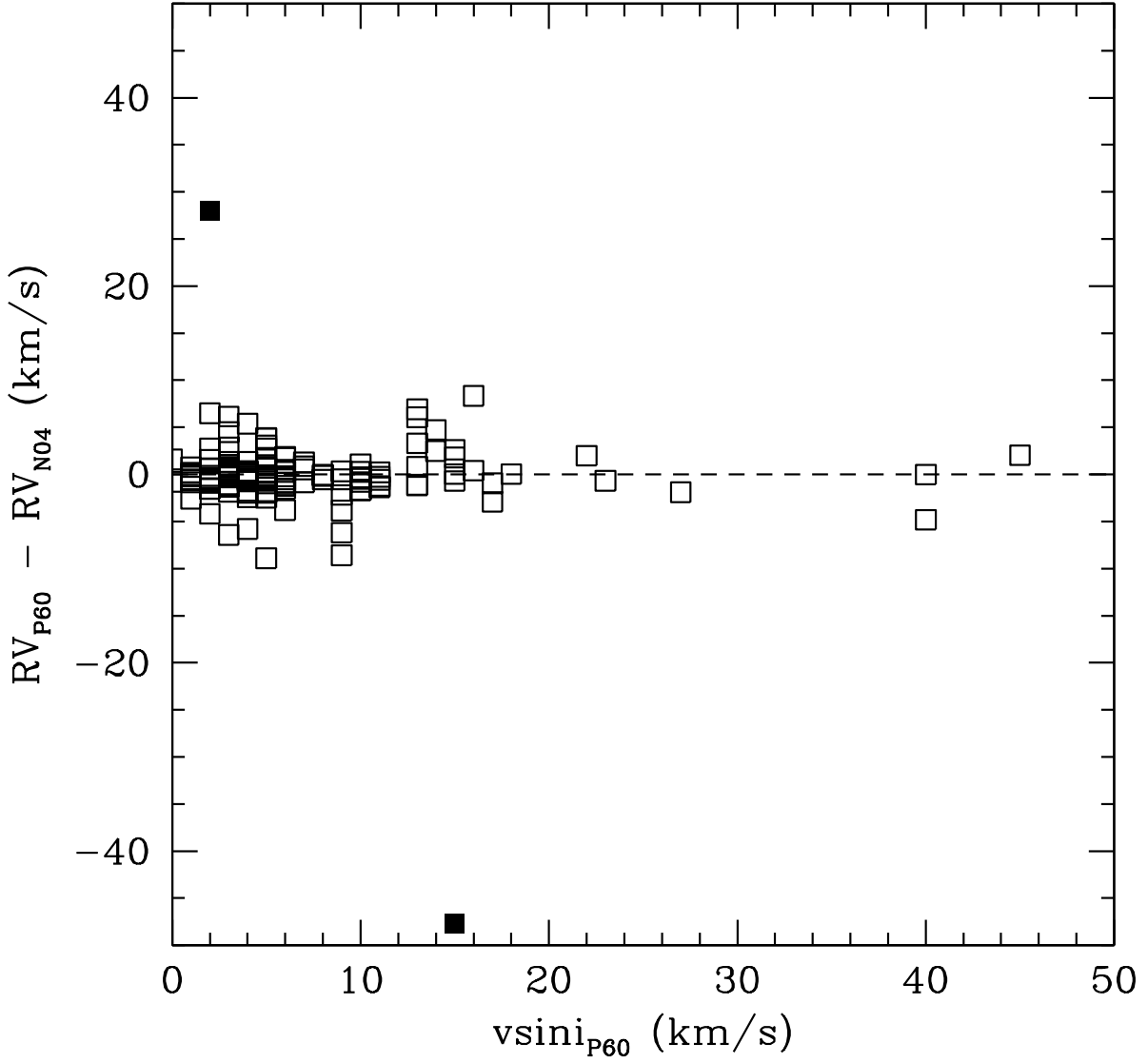


Fig. 6.— Difference between P60 radial velocities and values reported by Nordstrom et al. (2004). The *solid squares* are likely spectroscopic binaries.

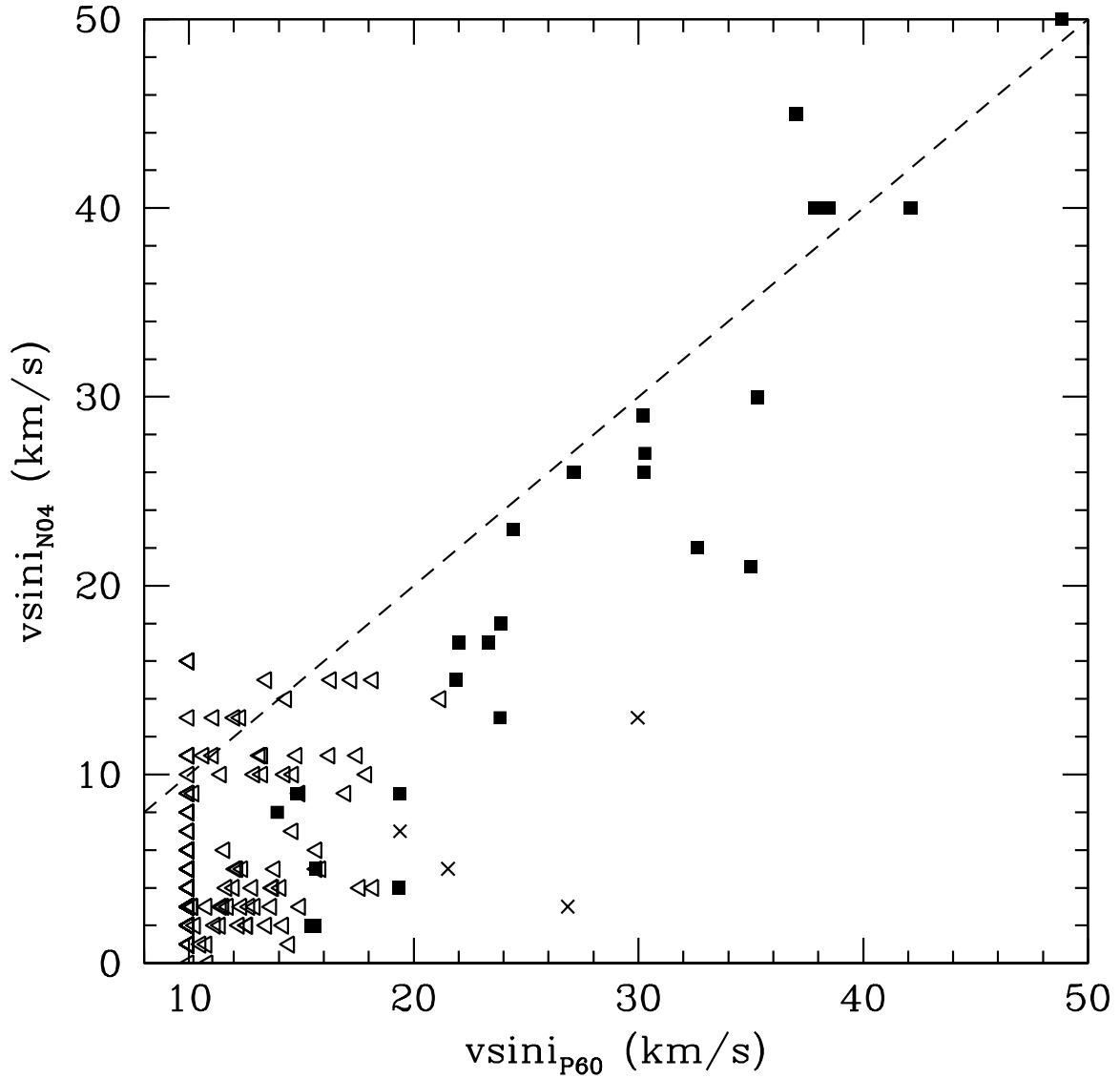


Fig. 7.— Comparison of measured $vsini$ values with values from Nordstrom et al. (2004). *Triangles* are upper limits and *squares* are measured values; Nordstrom et al. (2004) report no upper limits. The 3 *x*'s indicate measurements from the night of 2002 Feb 2, which had significant focus problems (Section 4.2).

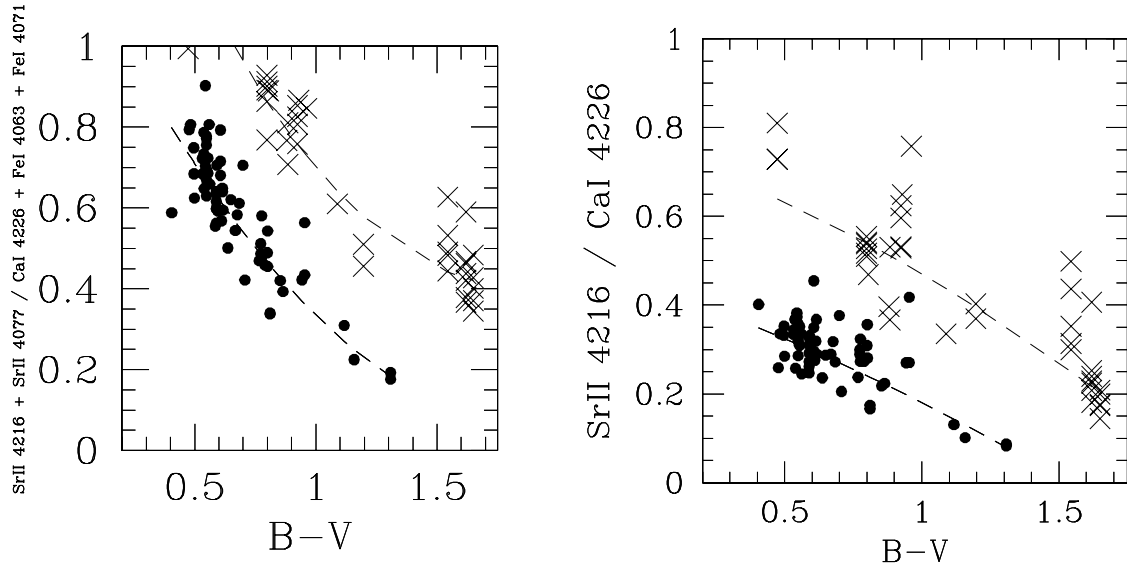


Fig. 8.— Gravity sensitive equivalent width ratios versus B-V color. Dwarf stars are indicated with *solid circles* and giant stars are indicated with *crosses*.

than one spectral subclass would result. Therefore we do *not* use these features to estimate spectral types. Spectral types instead are taken from several catalogues of stellar spectral classification, when available. These, in order of preference are Houk & Swift (1999), Skiff (2005), Kharchenko (2001), Kharchenko, Piskunov, Scholz (2004). The spectral types are listed in Table 1; 349 of the 370 stars observed have stellar spectral types.

For gravity indicators, we considered the ratios of the gravity sensitive Sr II $\lambda 4216$ and $\lambda 4077$ lines (see Jaschek & Jaschek 1987) to the above temperature sensitive lines. In Figure 8 we show for our dwarf and giant standard stars the ratios (Sr II $\lambda 4216 + \lambda 4077$) to (Ca I $\lambda 4226 + \text{Fe I } \lambda 4063 + \text{Fe I } \lambda 4071$) and Sr II $\lambda 4216$ to Ca I $\lambda 4226$, as a function of $B - V$ color. These ratios are sensitive to both temperature and gravity; the dwarf and giant stars are reasonably well separated in these plots. Parabolic fits to the dwarf and giant points are shown. The majority of our target objects cluster around the dwarf locus, though some are securely between the dwarf and giant loci. Other diagnostic figures, such as Sr II $\lambda 4077 / (\text{Fe I } \lambda 4063 + \text{Fe I } \lambda 4071)$ versus Ca I $\lambda 4226$, (which has the advantage of considering only our spectroscopic data), have similar appearances. In principle one might use such figures to quantitatively estimate the surface gravities of our program stars; in practice, however, the data do not allow this to be carried out with the precision normally expected of surface gravity measurements. Rather than estimate surface gravities, we simply identify all stars which are more than the 1σ above the dwarf loci in both diagnostic planes. Sixty-six potentially low surface gravity stars are identified by these criteria and marked in Table 1.

4.4. Chromospheric Ca II H and K Activity Measurements

Core emission in the Calcium H and K spectral lines serves as an indicator of stellar chromospheric activity, which is known to be correlated with stellar age (e.g. Soderblom et al. 1991), primarily as a consequence of rotation. We parameterize the core emission in our spectra using the standard Mount Wilson Project procedures (Wilson 1968; Vaughan et al. 1978). Our prescription for measuring the core emission closely follows that outlined by Duncan et al. (1991). First we define the index of core emission, S , as

$$S = \frac{N_H + N_K}{N_R + N_V}, \quad (1)$$

where N_i is the number of counts in band i . The continuum bands, R and V , are 20 \AA wide and centered at 4001.07 \AA and 3901.07 \AA , respectively. The emission bands, H and K , are centered on the emission features whose natural centers are at 3968.470 \AA and 3933.664 \AA , respectively. The bandpass for the H and K channels is triangular, with a full width at half maximum of 1.09 \AA . Before measuring the counts within these four bands, the spectra

are normalized to account for the blaze function and shifted to correct for radial velocity. The spectra are normalized in a two step iterative process. First, a ~ 4 th order polynomial is fit to the spectra; the broad H and K absorption features are excluded in this fit. A second polynomial is then fit to the spectra, excluding all spectral features that extend 0.5σ below the initial polynomial fit. The spectra are then normalized by dividing by this polynomial. The velocity shift is determined by cross-correlating the 2 spectra orders with the Ca II H and K features, with the spectrum of a bright comparison standard. The implied radial velocity is compared with that determined in Section 4.2 to ensure consistency; for the chromospheric activity analysis we adopted values determined directly from these orders as they typically provide the most accurate shift for these orders.

With velocity shifted and normalized spectra, the counts within the continuum and emission bands of the S index are summed. For the emission bands, the number of counts in each pixel is first multiplied by a number from 0 to 1 to mimic a triangular bandpass with a full-width at half-maximum of 1.09 \AA . With these sums, equation (1) is used to compute S .

To correct for systematic offsets in the measured S values relative to previous work, possibly due to slight differences in the methodology or data quality, the S values are compared to those measured by Wright et al. (2004, also appearing after all data for this program were gathered). These comparisons permit transformation of the S values to what we refer to as Mount Wilson S values, S_{MW} . This is realized as a first order regression analysis on $\log S$ in the form of

$$\log S_{MW} = A + B \log S. \quad (2)$$

The uncertainty, $\sigma_{S_{MW}}$, is given by the standard formula

$$\sigma_{S_{MW}}^2 = \left(\frac{\partial S_{MW}}{\partial A} \sigma_A \right)^2 + \left(\frac{\partial S_{MW}}{\partial B} \sigma_B \right)^2. \quad (3)$$

The analysis was performed on 8 of the 9 observing runs and for the entire overlapping sample; there were too few overlapping stars for the 2001 December observing run for comparison. Fortunately, the uncertainties in the implied correction estimates for 7 of the 8 observing runs agree well with that determined for the entire overlapping sample. The one exception was for the July 2001 observing run, for which the corrections appeared significantly different. Therefore, the corrections determined for this run were used to transform its S values to S_{MW} values, while the remaining runs used the corrections determined for the entire sample, which are more precise. The resulting Mount Wilson Calcium index values and uncertainties are listed in Table 1. Stars with uncertainties that are possibly much larger than reported, because of a large systematic uncertainty that is not formally propagated (e.g. radial velocity error) are marked with an "e" in Table 1.

Finally, the S_{MW} values are converted to R'_{HK} values, which express the activity as a fractional ratio with the underlying star, following the prescription described in Noyes et al. (1984). However, this conversion requires proper characterization of the underlying photospheric flux, which can be assessed from the intrinsic stellar $B - V$ color. $B - V$ colors for most stars are obtained from the Tycho-2 catalogue (Høg et al. 2000). These values are transformed to Johnson $B - V$ colors, following the relations in Mamajek et al. (2002)². For objects without Tycho photometry, the $B - V$ colors are estimated from the stellar spectral type (Section 4.3) following the relations of Johnson (1966).

R'_{HK} is calculated as the difference in the logarithms of the flux calibrated core emission, R_{HK} , and photospheric emission, R_{phot} :

$$R'_{HK} = R_{HK} - R_{phot}. \quad (4)$$

Here R_{HK} is calculated from the S_{MW} values and calibrated using the stellar $B - V$ color, and R_{phot} is calculated from the $B - V$ color alone (see Appendix b in Noyes et al. 1984 for explicit formulae). Although the calibration of these terms is determined over the restricted $B - V$ range of $0.44 < (B - V) < 0.82$, we use it for the full $B - V$ range of the observed sample ($0.19 < (B - V) < 1.65$). The resulting R'_{HK} values are listed in Table 1.

5. Sample Properties

5.1. Spectroscopic Binaries

Table 2 lists the 8 stars with photospheric spectral features that are doubled in our observations. Two of these double-lined spectroscopic binaries were previously known (HE 848, SAO 178 272), while HD 78899, TYC 7310 503 1, TYC 7305 380 1, and HD 140374 are newly identified. The multiple epoch observations of some stars also allows us to identify single-lined binaries based on changes in radial velocity. We consider an object a candidate binary if its radial velocity changed by more than 10σ between observations; 3 stars meet this criteria: HD92855 (HIP52498), HD132173 (HIP73269), HD61994 (HIP38018; see Table 1). Similarly, based on comparisons with radial velocities published in Nordstrom et al. (2004), HD108944 (HIP61072) and HD121320 (HIP67904) are candidate binaries (see Figure 6). All 5 are newly identified candidate binary systems. Finally, since the radial velocity dispersion in young clusters is typically $< 2 \text{ km s}^{-1}$, comparison of cluster member radial velocity

²There is a typographical error in the relations of Mamajek et al. (2002). The +0.007813 in equation C6 should be -0.007813.

measurements with the median cluster values can identify single-lined spectroscopic binaries. Based on these comparisons, the two Pleiades members HII 571 and LH98 103 are identified as spectroscopic binaries; both have been identified previously as such (Mermilliod et al. 1992; Queloz et al. 1998).

5.2. Sample Age Dispersion

Several of the quantities extracted from the observed spectra are likely to be correlated with stellar age, based on extensive studies in the literature. Generally speaking, younger stars tend to be more rapidly rotating, have larger lithium abundances, and have stronger chromospheric emission lines such as Ca II H&K and H α . Thus the measured quantities $v \sin i$, EW[Li I λ 6708], $\log R'_{HK}$, and EW[H α] should correlate with age. Unfortunately the precision with which stellar ages can be estimated from these quantities is in general poor, in part because of the additional dependencies upon stellar spectral type and rotation. Rather than attempting to disentangle these complicating effects for individual stars, we simply present the data to illustrate the empirical correlations amongst the measured quantities and to assess the overall age range of the observed sample.

Figure 9 shows the distributions of EW[Li I 6708], EW[H α] and $v \sin i$ versus $\log R'_{HK}$. Error bars are not displayed due to crowding, but can be inferred from the information in Table 1. The EW[Li I] and $\log R'_{HK}$ values are reasonably well correlated, as expected if strong lithium absorption and strong chromospheric emission, as traced by Ca II emission, both indicate stellar youth. The EW[H α] and $\log R'_{HK}$ values are at best weakly correlated; stars with larger $\log R'_{HK}$ values have, on average, smaller EW[H α] values, suggesting they are partially filled in by emission. The strong spectral type dependence of this temperature sensitive line likely masks much of the underlying correlation which might be revealed by considering an analogously defined quantity $R'_{H\alpha}$. The $v \sin i$ values are well correlated, in the mean, with $\log R'_{HK}$ values. This is expected since increased rotation is believed to cause increased chromospheric activity, a characteristic common in young stars. Finally, in Figure 10 are shown the distributions of EW[H α] and $v \sin i$ versus EW[Li I]. Both the EW[H α] and $v \sin i$ values are correlated with EW[Li I], in the mean, though both show a large scatter at all EW[Li I] values.

The above correlations corroborate the suggestion that these measured quantities trace stellar age. While the large scatter in these correlations inhibits assigning specific ages to individual stars, the ensemble distributions can help assess the age of the observed sample. Since the stellar temperature can also affect these quantities, we consider these distributions as a function of $B - V$ color, a proxy for stellar temperature. The range of observed values at

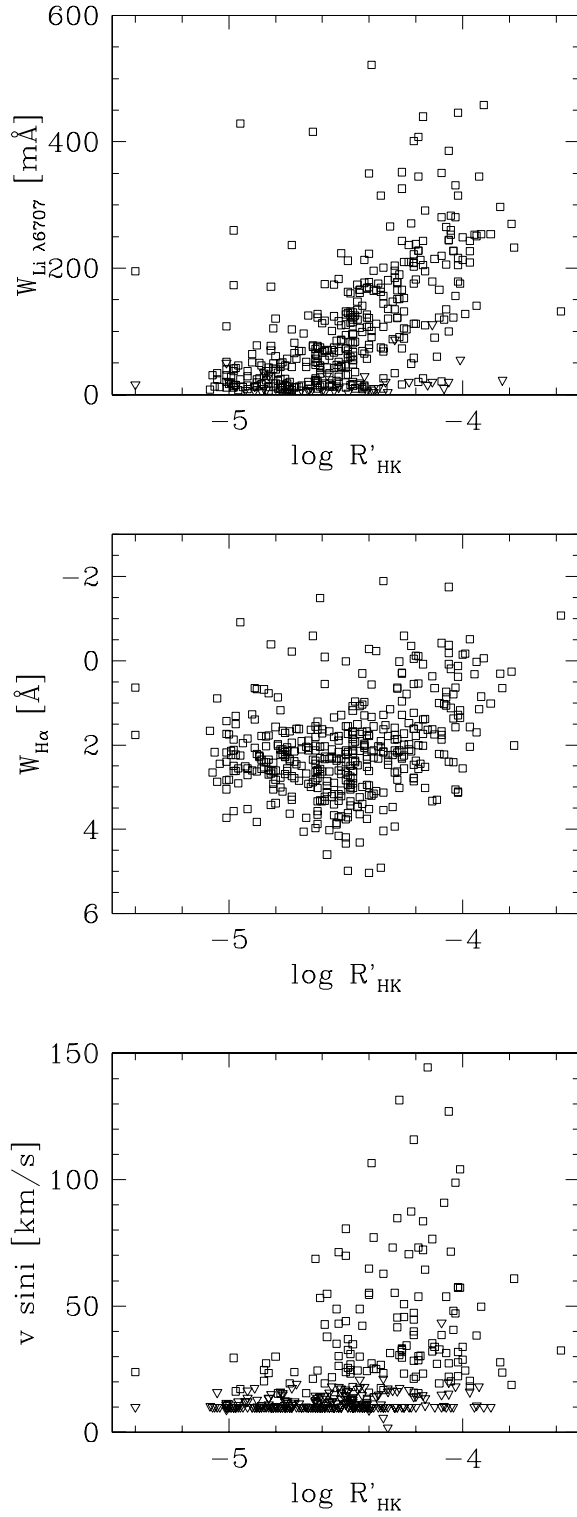


Fig. 9.— EW[Li I 6708], EW[H α] and $v \sin i$ versus the chromospheric activity diagnostic $\log R'_{HK}$. Measured values are shown as *squares* while upper limits are shown as *triangles*.

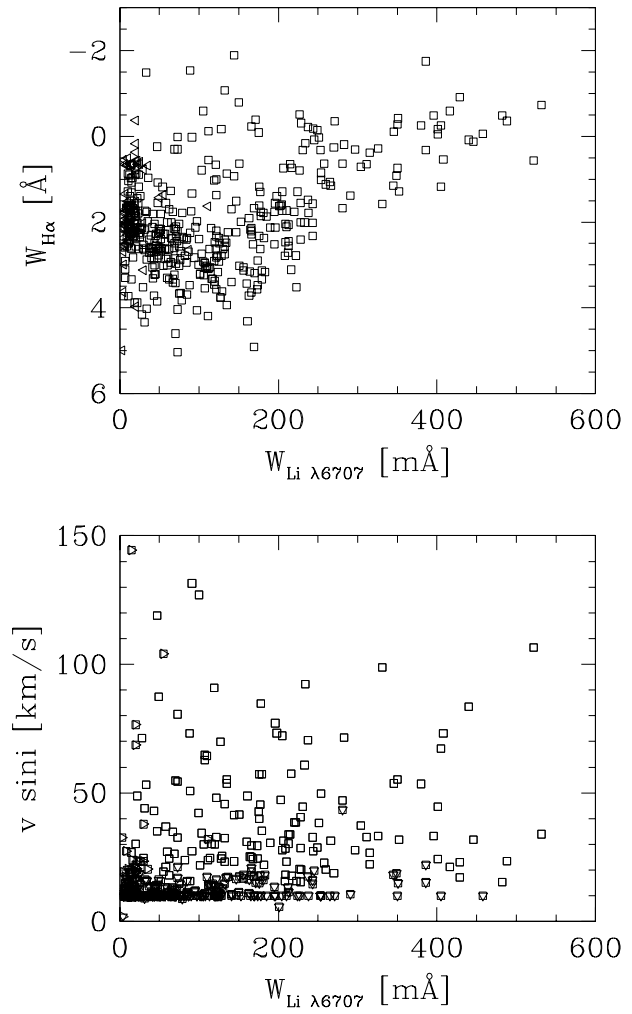


Fig. 10.— $\text{EW}[\text{H}\alpha]$ and $v \sin i$ versus the $\text{EW}[\text{LiI } 6708]$. Measured values are shown as *squares* while upper limits are shown as *triangles*.

any $B - V$ color should therefore (mostly) be a consequence of the age spread in the sample; a comparison of the spread of values at different colors can serve as a check for age biases with respect to temperature.

In Figure 11 are shown the distributions of $v \sin i$, $\text{EW}[\text{Li I } \lambda 6708]$, $\log R'_{HK}$, and $\text{EW}[\text{H}\alpha]$ versus $B - V$ color (as assembled in Section 4.4). The observed dwarf standards are distinguished in order to illustrate the properties of old slowly rotating stars. The distributions of $v \sin i$ and $\log R'_{HK}$ are independent of $B - V$ color, indicating a similar spread in rotation rate and chromospheric activity over the range of spectral types observed. The $\text{EW}[\text{Li I}]$ values span a broad range at each $B - V$ color. The larger $\text{EW}[\text{Li I}]$ values at the red end is a temperature effect; for a specified lithium abundance, the $\text{EW}[\text{Li I}]$ increases with decreasing stellar temperature (Pavlenko & Magazzú 1996). The $\text{EW}[\text{H}\alpha]$ values show the strongest $B - V$ trend, as expected for this temperature sensitive line; the $\text{EW}[\text{H}\alpha]$ values decrease with increasing $B - V$ color. There is also a larger scatter at larger $B - V$ values. The scatter above the dwarf loci can be interpreted as stars with some $\text{H}\alpha$ emission, whether this is partially or completely (e.g. $\text{EW}[\text{H}\alpha] < 0.0$) filling in the photospheric absorption line. Four stars with strong $\text{H}\alpha$ emission ($\text{EW}[\text{H}\alpha] > -10 \text{ \AA}$) are not plotted; their profiles are shown in Figure 4. Stars with some $\text{H}\alpha$ emission span the full range of $B - V$ colors, though there appear to be many more at redder colors ($B - V > 1.0$) than bluer colors ($B - V < 0.6$). However, since an EW is defined relative to the continuum flux, a unique $\text{EW}[\text{H}\alpha]$ value corresponds to much less $\text{H}\alpha$ flux for cooler (red) stars than hotter (blue) stars. Overall, these age indicators are consistent with the observed sample having ages that span from a few million years to a few billion years, as was intended. Moreover, all spectral types appear to span this range of ages; there is no strong age bias with spectral type amongst the observed sample.

5.3. Ca II H&K Saturation in Young Stars

While $\log R'_{HK}$ values have been shown to correlate with stellar age (e.g. Soderblom et al. 1991), this diagnostic typically has not been used to estimate ages less than ~ 100 Myr. This primarily stems from the lack of R'_{HK} measurements for stars in young clusters of known age, from which the age relation could be calibrated. Although the P60 R'_{HK} measurements of young cluster members presented here may help establish this calibration, we illustrate that accurate ages will be inhibited by the broad range in rotation rates for stars at a given young age and the saturation of flux at high rotation rates.

In Figure 12 are shown the R'_{HK} measurements versus projected rotational velocity ($v \sin i$) of stars in the open clusters represented in our sample, including α Persei, the

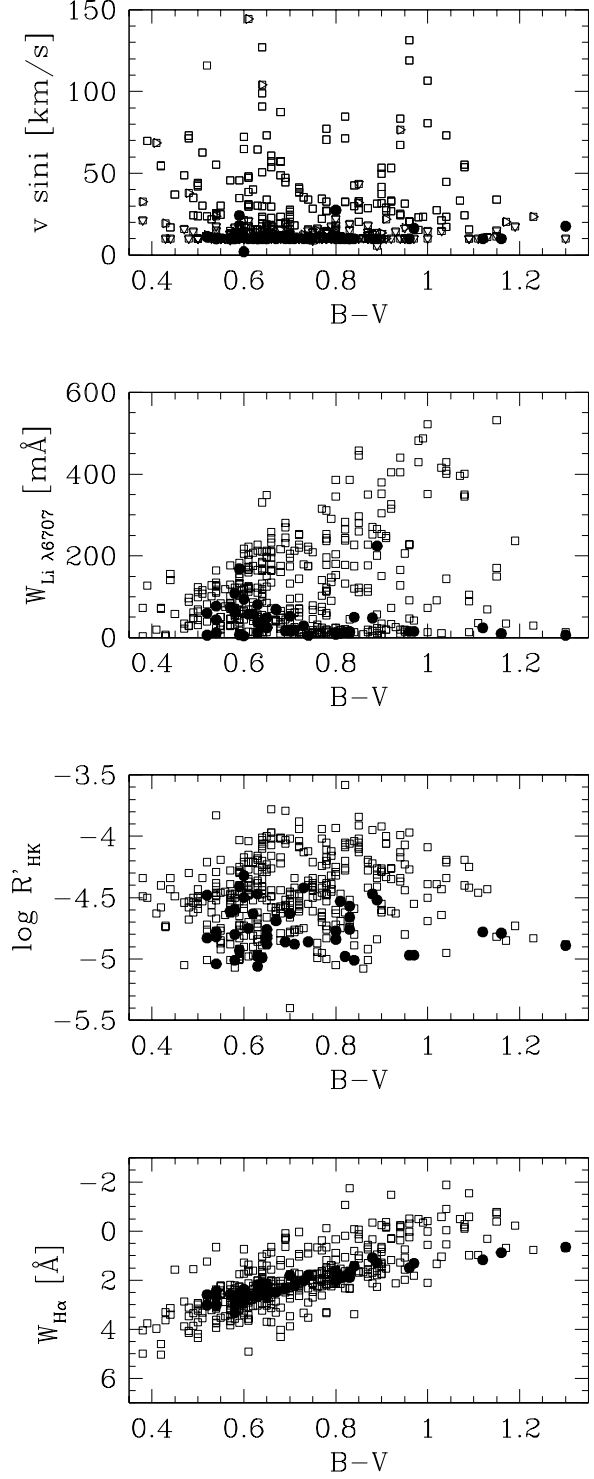


Fig. 11.— Projected rotational velocity ($v \sin i$), $\text{EW}[\text{Li } \lambda 6708]$, $\log R'_{\text{HK}}$ and $\text{EW}[\text{H}\alpha]$ versus $B - V$ color. *Filled circles* indicate dwarf standard stars. For clarity, a few stars in the observed sample are bluer than (SAO 41857) or redder than (HIP 108467, HIP 90190, and HIP 60783) the $B - V$ range shown here, the values are nevertheless included in Table 1. Similarly, in the bottom panel four stars with strong $\text{H}\alpha$ emission ($\text{EW}[\text{H}\alpha] < -10$; Figure 4) are not shown.

Pleiades, the Hyades and collectively (post) T Tauri stars in Upper Scorpius, Upper Centaurus Lupus, and R Corona Australis. As expected, the R'_{HK} measurements are correlated with $v \sin i$; the most rapidly rotating stars have, on average, the largest R'_{HK} values. However, Figure 12 also indicates that once the $v \sin i$ values increase above $\sim 30 \text{ km s}^{-1}$, the R'_{HK} values stay roughly constant, implying no increase in the Ca II H&K emission line flux toward larger rotation rates. A similar “saturation” phenomenon has been seen before based on observations of other emission lines originating in stellar chromospheres (OI 1304, C II 1335), as well as X-rays originating in stellar corona (e.g. Vilhu 1984). It is not yet known whether the cause for flux saturation is internal (e.g. dynamo) or external (e.g. active regions) to the star (see Güdel 2004). Saturation of the Ca II H&K fluxes, as measured by the R'_{HK} diagnostic, has not been demonstrated before.

While saturation of the Ca II H&K flux seems consistent with other chromospheric and coronal observations of rapidly rotating stars, we considered the possibility that this saturation is simply a consequence of the method used to determine the S values, which are used to calculate R'_{HK} . Specifically, since the prescription outlined in Section 4.4 involves measuring the Ca II K and H emission with a triangular passband of specified width, apparent saturation could be caused by emission line flux being rotationally broadened outside of this passband, and thus not included in the measurement. To test this, we remeasured S values for a set of stars that were artificially rotationally broadened from 10 to 150 km s^{-1} ; we assume the core emission is rotationally broadened by the same amount as the photosphere. This showed that the technique used to measure the S values begins to miss core emission flux above $v \sin i$ of $\sim 100 \text{ km s}^{-1}$. Since the saturation observed for R'_{HK} occurs well below this value, we interpret the saturation as a real effect.

To further demonstrate the case for saturation, in Figure 12 we also illustrate the ratio of X-ray flux to bolometric flux (L_X/L_{bol}) for the stars in these clusters which have the available data. X-ray fluxes are from ROSAT observations and bolometric fluxes are determined from the atmospheric model which best fits the stellar energy distribution (see Mamajek et al. 2007 for a complete description of the L_X/L_{bol} derivation). A saturation trend is identified for coronal X-rays similar to that for chromospheric Ca II H&K core emission. The most rapidly rotating stars are the most fractionally X-ray bright, but L_X/L_{bol} remains roughly constant above $v \sin i$ values of $\sim 30 \text{ km s}^{-1}$. This phenomenon has been demonstrated previously by many authors. What we have newly demonstrated here is that the same young cluster stars that have saturated X-ray emission also have saturated chromospheric Ca II H&K emission.

We are grateful to the observing assistants formerly present at the Palomar 60-inch, Karl Dunscombe and Skip Staples, for their help and patience in acquiring this large data set. We thank E. Mamajek and C. Slesnick for assisting with the observations and Jonathan

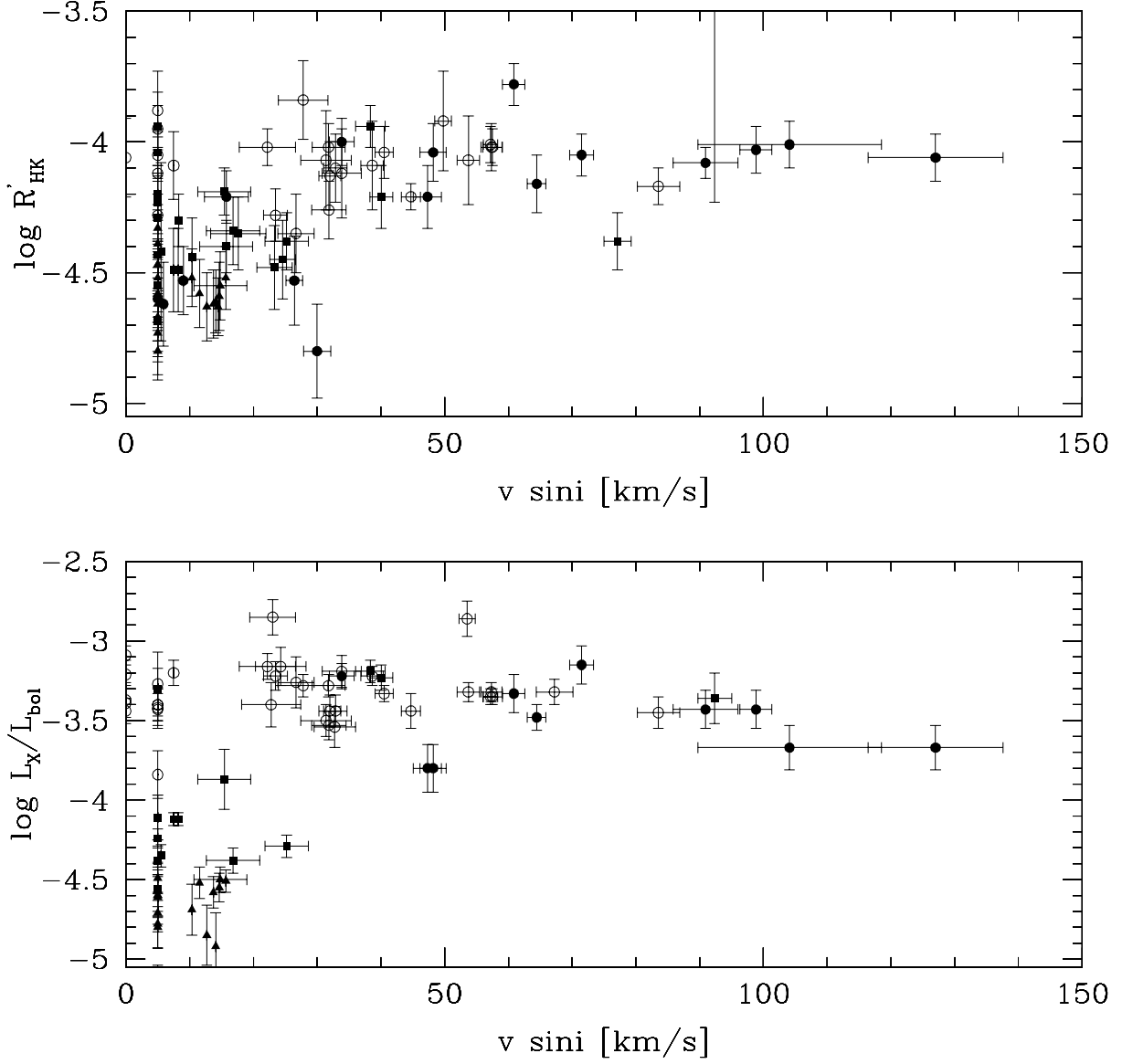


Fig. 12.— R'_{HK} and L_X/L_{Bol} measurements of open cluster members versus $v \sin i$. *Filled circles* are α Per members, *squares* are Pleiads, *triangles* are Hyads and *open circles* are T Tauri stars in Upper Scorpius, Upper Centaurus Lupus, and R Corona Australis. Stars with a $v \sin i$ upper limit are plotted with a $v \sin i$ of 5 km s^{-1} for clarity.

Foster, Francesca Colonnese, and Michael Inadomi for their assistance with data reduction and analysis. We appreciate greatly the scattered light analysis provided by J. Valenti for some of our spectra. This research has made use of the SIMBAD and 2MASS databases. We acknowledge support for these observations from NASA contract 1224566 administered through JPL. This work has benefited from the ability to organize our data within the FEPS database created by John Carpenter.

REFERENCES

- Cutri, R. M. et al. 2003, The IRSA 2MASS All-Sky Point Source Catalog, NASA/IPAC Infrared Science Archive
- Duncan, D. K., et al. 1991, *ApJS*, 76, 383
- Gray, D. 1992, *The Observation and Analysis of Stellar Photospheres* (Cambridge: Cambridge University Press)
- Güdel, M. 2004, *ARA&A*, 12, 71
- Høg, E., et al. 2000, *A&A*, 357, 367
- Jaschek, C. & Jaschek, M. 1987, *The Classification of Stars* (Cambridge: Cambridge University Press)
- Johnson, H. L. 1966, *ARA&A*, 4, 193
- Mamajek, E. E., Meyer, M. R. & Liebert, J. 2002, *AJ*, 124, 1670
- McCarthy, J. K. 1988, Ph.D. thesis, California Institute of Technology
- Mermilliod, J. -C., Rosvick, J. M., Duquennoy, A. & Mayor, M. 1992, *A&A*, 265, 513
- Muzerolle, J., Calvet, N. & Hartmann, L. 1998, *ApJ*, 492, 743
- Meyer, M. R., et al. 2006, *PASP*, in press
- Nidever, D. L., Marcy, G. W., Butler, R. P., Fischer, D. A. & Vogt, S. S. 2002, *ApJS*, 141, 503
- Nordstrom, B., et al. 2004, *A&A*, 418, 989
- Noyes, R. W., Hartmann, L. W., Baliunas, S. L., Duncan, D. K., & Vaughan, A. H., 1984, *ApJ*, 279, 763.
- Ochsenbein, F., Bauer, P., & Marcout, J. 2000, *A&AS*, 143, 23
- Pavlenko, Y. V. & Magazzú, A. 1996, *A&A*, 311, 961
- Queloz, D., Allain, S., Mermilliod, J. -C, Bouvier, J. & Mayor, M. 1998, *A&A*, 335, 183
- Soderblom, D. R., Duncan, D. K. & Johnson, D. R. H. 1991, *ApJ*, 375, 722

- Soderblom, D. R., Jones, B. F., Balachandran, S., Stauffer, J. R., Duncan, D. K., Fedele, S. B., Hudon, J. D. 1993, *AJ*, 106, 1059
- Strassmeier, K., Washuettl, A., Granzer, Th., Scheck, M. & Weber, M. 2000, *A&AS*, 142, 275
- Thorburn, J. A., Hobbs, L. M., Deliyannis, C. P. & Pinsonneault, M. H. 1993, *ApJ*, 415, 150
- Vaughan, A. H., Preston, G. W. & Wilson, O. C. 1978, *PASP*, 90, 267
- Vilhu, O 1984, *A&A*, 133, 117
- Vogt, S. S., et al. 1994, *Proc. SPIE*, 2198, 362
- White, R. J. & Hillenbrand, L. A. 2004, *ApJ*, 616, 998
- White, R. J. & Basri, G. 2003, *ApJ*, 582, 1109
- Wichmann, R., Schmitt, J. H. M. M., Hubrig, S. 2003, *A&A*, 399, 983
- Wilson, O. C. 1968, *ApJ*, 153, 221
- Wright, J. T., Marcy, G. W., Butler, R. P. & Vogt, S. S. 2004, *ApJS*, 152, 261

Table 1. Spectroscopic Properties of Observed Single(-Lined) Stars

HD	HIP	other	Grp	RA(2000)	DEC(2000)	Epoch	SNR <i>atLi</i>	EW[LiI] (Å)	EW[H α] (Å)	RV (km s ⁻¹)	vsini (km s ⁻¹)	SNR <i>atHK</i>	S_{MW}^a	Spectral Type ^b	B-V ^c
224873	110	RX J0001.4+3936	Field	00 01 23.66	+39 36 38.1	2001 Dec 2	105	0.032	1.74	-5.6 ± 1.4	< 16.3	50	0.365 0.068	K0	0.76t
105	490	RX J0005.9-4145	Field	00 05 52.55	-41 45 10.9	2001 Dec 2	217	0.156	3.06	1.6 ± 1.2	< 18.2	16	0.675e 0.118	G0V	0.59t
377	682	1RXS J000826.8+063712	Field	00 08 25.74	+06 37 00.5	2001 Jul 27	348	0.122	2.34	-3.8 ± 2.2	< 12.0	135	0.348 0.12	G2V	0.63t
691	919	V344 And	Field	00 11 22.40	+30 26 58.4	2002 Oct 29	256	0.122	2.20	-2.4 ± 0.8	< 10.	84	0.388 0.072	K0V	0.78t
						2002 Sep 18	174	0.115	2.14	-3.0 ± 0.8	< 13.7	84	0.391 0.073	"	0.78t
984	1134	1RXS J001410.1-071200	Field	00 14 10.25	-07 11 57.0	2001 Jul 27	315	0.099	2.99	-3.2 ± 2.2	42.1 ± 1.7	131	0.296 0.104	F7V	0.50t
1326A	1475	GJ 15 A	Mstar	00 18 22.57	+44 01 22.2	2002 Oct 30	198	< 0.01	0.51	12.0 ± 0.9	< 20.5	38	0.568 0.101	M2V	1.48t
1326B	...	GJ 15 B	Mstar	00 18 25.50	+44 01 37.6	2002 Oct 30	87	< 0.02	0.17	10.7 ± 0.9	< 18.9	14	1.083 0.181	M5V	1.61s
3765	3206	GJ 28	Field	00 40 49.29	+40 11 13.3	2002 Sep 17	259	0.015	1.31	-63.8 ± 0.7	16.3 ± 5.1	65	0.218 0.043	K2V	0.97t
...	...	QT And	Field	00 41 17.32	+34 25 16.8	2002 Oct 29	160	0.128	-0.17	6.0 ± 0.8	24.4 ± 2.2	40	1.617 0.259	G	0.94t
						2002 Sep 18	83	0.166	-0.23	5.1 ± 0.7	25.1 ± 2.2	27	0.705 0.123	"	0.94t
6434	5054	GJ 9037	Field	01 04 40.15	-39 29 17.4	2001 Dec 2	231	< 0.004	2.37	21.9 ± 1.2	< 10.	28	0.396 0.074	G2/3V	0.60t
6963	5521	SAO 36995	Field	01 10 41.92	+42 55 54.7	2002 Sep 17	206	< 0.003	2.05	-31.7 ± 0.7	< 12.58	77	0.226 0.045	G7V	0.73t
7661	5938	SAO 147702	Field	01 16 24.18	-12 05 49.3	2003 Feb 8	185	0.075	2.04	5.2 ± 0.4	< 10.	33	0.479 0.087	K0V	0.77t
...	6276	SAO 147747	Field	01 20 32.26	-11 28 03.6	2003 Feb 8	178	0.153	1.99	8.3 ± 0.4	< 10.	29	0.619 0.110	G0	0.80t
8467	6575	SAO 54666	Field	01 24 27.98	+39 03 43.6	2002 Sep 17	172	< 0.011	1.64	15.0 ± 0.7	< 10.	60	0.278 0.054	G5	0.77t
8941	6869	SAO 92453	Field	01 28 24.36	+17 04 45.2	2001 Jul 29	421	0.006	2.59	9.3 ± 2.2	< 10.96	181	0.175 0.035	F8IV-V	0.52t
						2002 Sep 18	233	< 0.004	2.69	8.29 ± 0.70	< 12.3	123	0.190 0.069	F8IV-V	0.52t
8907	6878	IRAS 01256+4200	Field	01 28 34.35	+42 16 03.8	2001 Jul 26	266	0.048	1.55	6.3 ± 2.2	< 14.34	142	0.263 0.093	F8	0.49t
9472	7244	SAO 74789	Field	01 33 19.03	+23 58 32.1	2002 Sep 18	190	0.055	2.28	10.9 ± 0.7	19.33 ± 4.22	83	0.277 0.053	G0	0.68t
...	...	RX J0137.6+1835	Field	01 37 39.41	+18 35 33.2	2001 Jul 28	194	0.416	-0.59	1.8 ± 2.2	21.25 ± 3.26	26	0.512e 0.171	K3Ve	1.03t
10780	8362	IRAS 01441+6336	Field	01 47 44.88	+63 51 09.1	2001 Jul 28	203	0.012	1.66	1.4 ± 2.2	< 10.	55	0.237 0.085	K0V	0.80t
11850	9073	SAO 75038	Field	01 56 47.28	+23 03 04.1	2002 Oct 29	176	0.018	2.32	3.3 ± 0.8	< 12.08	54	0.287 0.055	G5	0.69t
						2002 Sep 18	138	0.015	2.27	1.6 ± 0.7	< 12.38	76	0.292 0.056	"	0.69t

^aStars with especially uncertain S values are marked with an "e".

^bStars which appear low surface gravity are marked with an asterisk.

^cB-V colors from the Tycho catalogue are marked with a "t" while those from the stellar spectral type are marked with an "s".

^dStars with B-V colors outside the range over which R'_{HK} values are calibrated are marked with a "c".

Table 2. Observed Double-Lined Binary Stars

HD	HIP	other	Assoc	RA(2000)	DEC(2000)	Epoch	SNR <i>atLi</i>	EW[LiI] (mÅ)	EW[Ca I] (mÅ)	EW[H α] (Å)
...	...	Cl Melotte 20 848	aPer	03 29 26.24	+48 12 11.74	2002 Oct 31	149	45/69	61/85	1.65/0.95
78899	45187	GJ 3539	Field	09 12 28.24	+49 12 23.4	2003 Feb 9	260	11/50	91/121	0.83/0.72
...	...	SAO 178272	Field	09 59 08.42	-22 39 34.57	2002 Feb 4	107	87/162	105/153	em.
"	"	"	"	"	"	2001 Dec 2	134	em.
"	"	"	"	"	"	2002 Apr 19	51	103/204	174/233	-0.1/-0.2
...	...	TYC 7310 503 1	Field	14 58 37.69	-35 40 30.27	2003 Jun 5	82	121/222	99/180	em.
...	...	TYC 7305 380 1	Field	14 50 25.82	-35 06 48.66	2002 Feb 3	85	132/250	103/66	...
"	"	"	"	"	"	2003 Jun 5	79	307/60	120/54	...
140374	77081	TYC 7331 1235 1	Field	15 44 21.06	-33 18 54.97	2003 Jun 4	145	112/116	61/77	-0.96/-1.17
142229	77810	SAO 121238	Field	15 53 20.01	+04 15 11.5	2002 Feb 2	119	56/121	29/79	...
218738	114379	KZ And	Field	23 09 57.34	+47 57 30.0	2003 Jun 6	73	69/107	108/165	...